IEEE Access
Multidisciplinary ⁝ Rapid Review ⁝ Open Access Journal

Received 5 October 2022, accepted 4 November 2022, date of publication 14 November 2022, date of current version 23 November 2022.

Digital Object Identifier 10.1109/ACCESS.2022.3222313

RESEARCH ARTICLE

Improved Dynamic Contrast-Enhanced MRI Using Low Rank With Joint Sparsity

JICHANG ZHANG[1,2], **FAISAL NAJEEB**[3,4], **XINPEI WANG**[1], **PENGFEI XU**[1], **HAMMAD OMER**[3], **JIANJUN ZHENG**[5,6], **JINGFENG ZHANG**[5,6], **SUE FRANCIS**[4], **PAUL GLOVER**[4], **RICHARD BOWTELL**[4], **AND CHENGBO WANG**[1,7]

[1]Faculty of Science and Engineering, University of Nottingham Ningbo China, Ningbo 315100, China
[2]XinGaoYi Medical Equipment Company Ltd., Yuyao 315400, China
[3]MIPRG Research Group, Department of Electrical and Computer Engineering, COMSATS University Islamabad, Islamabad 45550, Pakistan
[4]Sir Peter Mansfield Imaging Centre, University of Nottingham, NG7 2RD Nottingham, U.K.
[5]Ningbo Clinical Medical Research Center of Imaging Medicine, Ningbo 315010, China
[6]Hwa Mei Hospital, University of Chinese Academy of Sciences, Ningbo 315010, China
[7]Nottingham Ningbo China Beacons of Excellence Research and Innovation Institute, Ningbo 315040, China

Corresponding author: Chengbo Wang (chengbo.wang@nottingham.edu.cn)

This work was supported in part by XGY Medical Equipment Company, Yuyao, China; in part by the National Key Research and Development Program of China under Grant 2019YFC0118700 and Grant 2022YFC2408900; in part by the Ningbo "S&T Innovation 2025" Major Program under Grant 2022Z141; and in part by the Ningbo Clinical Research Center for Medical Imaging under Grant 2021L003.

ABSTRACT This work presents a free-breathing dynamic contrast-enhanced (DCE) MRI reconstruction method called low-rank plus sparse (L+S) with joint sparsity. The proposed method improved dynamic contrast performance by integrating an additional temporal Fast Fourier Transform (FFT) constraint into the standard L+S decomposition method. In the proposed method, both temporal total variation (TV) sparsity constraint and temporal FFT constraint are integrated into a standard L+S decomposition model, forming L+S with joint sparsity. Temporal TV and Temporal FFT aim to suppress under-sampling artifacts and improve dynamic contrast in DCE-MRI, respectively. A fast composite splitting algorithm (FCSA) is adopted for solving the L+S model with multiple sparsity constraints, maintaining the reconstruction efficiency. A computer simulation framework was developed to compare the performance of L+S with joint sparsity and other reconstruction schemes. The performance of L+S with joint sparsity was tested using computer simulation and several liver DCE-MRI datasets. The proposed L+S based method achieved around four times faster reconstruction speed than the GRASP method. With the support of an additional sparsity constraint, the peak DCE signal in the proposed method was increased by more than 20% over that of a standard L+S decomposition.

INDEX TERMS Compressed sensing, DCE-MRI, dynamic contrast, joint sparsity, parallel imaging, reconstruction efficiency.

I. INTRODUCTION

Dynamic contrast-enhanced (DCE) MRI possesses an unparalleled capacity for detecting tumors and other lesions [1], [2], [3], [4]. Typically, multiple three-dimensional (3D) MRI images are rapidly acquired with different contrast-enhancement phases for monitoring fast signal-intensity changes [5], [6], [7]. The demand for rapid imaging speed with high spatial and temporal resolutions is challenging for MRI hardware, potentially limiting its clinical applications.

The general parallel imaging acceleration techniques, including sensitivity encoding (SENSE) [8] and generalized autocalibrating partially parallel acquisitions (GRAPPA) [9], employ spatial information from multiple receiver coils with sensitivity maps to reconstruct the under-sampled dataset. The acceleration factor (AF) in parallel imaging is limited by the degradation of the signal-to-noise ratio (SNR) [10]. Compressed sensing is another technique that has already shown great potential to overcome the limitations of general

The associate editor coordinating the review of this manuscript and approving it for publication was Qingli Li.

acceleration techniques like AF, spatial and temporal resolutions, etc. [11], [12]. Compressed sensing for dynamic MRI imaging is implemented based on the fact that continuously acquired image series express sparsity in the temporal domain with appropriate sparsity transforms like temporal total variation (TV) [13], [14], [15]. Golden angle radial sparse parallel (GRASP) combines the temporal incoherence of stack-of-stars golden angle radial sampling pattern and acceleration capability of parallel imaging and compressed sensing for highly accelerated free-breathing DCE-MRI reconstruction [16]. Golden angle radial sampling enables a relatively uniform coverage of k-space among subdivided time series. It simultaneously induces sampling incoherence on the temporal dimension [17], [18]. The non-linear conjugate gradient (NLCG) algorithm [19] can be employed to obtain the optimal solution for the GRASP model. A variety of research work has demonstrated the high performance of GRASP for free-breathing imaging of body tissues like the abdomen and prostate [16], [20], [21]. However, the repeated gridding/degridding procedures in NLCG result in an excessively long reconstruction period [22].

Besides the GRASP based techniques, combining compressed sensing and low-rank completion is widely adopted in reconstructing highly under-sampled dynamic MRI [23], [23], [24], [25]. Low-rank plus sparse (L+S) decomposition approach decomposes the time series further into low-rank background components L and sparse dynamic components S [26], [27]. A sparser representation of S is achieved in an appropriate transform domain, offering higher temporal fidelity and better tissue contrast at high AF [24]. The iterative shrinkage-thresholding algorithm (ISTA) [28] provides a faster convergence speed in L+S decomposition than NLCG in GRASP. Consequently, high reconstruction efficiency has been achieved by standard L+S decomposition.

Besides the reconstruction efficiency, dynamic contrast performance is crucial for clinical diagnosis. Both L+S decomposition and GRASP based techniques typically employ temporal TV as a sparsity transform to promote sparsity among multi-coil datasets [24], [29], [30]. Temporal TV can suppress all temporal variations, including temporally incoherent under-sampling artifacts. However, it also leads to the temporal averaging effect, which degrades the ultimate dynamic contrast of DCE-MRI.

In this work, we have integrated an additional sparsity constraint, "temporal fast Fourier transform (FFT)," into the standard L+S decomposition model with temporal TV, named "L+S with joint sparsity," to maintain the high reconstruction efficiency, suppress under-sampling artifacts and improve the dynamic contrast for DCE-MRI simultaneously. A fast composite splitting algorithm (FCSA) is applied to recover the desired image series from the L+S model with two sparsity constraints (temporal TV and temporal FFT) efficiently [31], [32]. We also developed a computer simulation framework to evaluate the performance of different reconstruction schemes.

More details about this research can be found in the author's Ph.D. thesis [33].

II. METHODS

The proposed "L+S with joint sparsity" method is an extension of L+S decomposition to include an additional temporal FFT constraint and FCSA. The objective of the proposed method is to deliver a new free-breathing DCE-MRI reconstruction framework, as shown in Figure 1, providing higher reconstruction efficiency and improved dynamic contrast simultaneously.

A. L+S WITH JOINT SPARSITY MODEL

The dynamic MRI dataset can be regarded as a superposition of low-rank background components which slowly vary over time and sparse dynamic components which rapidly vary along the temporal dimension. By combining compressed sensing and low-rank completion, a reconstruction model, "k-t SLR," is developed for dynamic MRI, while this model is challenging to optimize [24], [34]. L+S decomposition is developed based on both low-rank and sparse models to express the dynamic MRI dataset more efficiently [24].

In L+S decomposition, the acquired time series of the dynamic MRI dataset is converted into a space-time (y-t) matrix$M$. Each column of M presents a temporal frame. By applying singular value decomposition (SVD) and singular value thresholding (SVT) to M, a low-rank y-t matrix L is extracted from the M. Lcontains a few non-zero singular values and presents the slowly varying background components. The sparse y-t matrix S is obtained by subtracting the original matrix M with the low-rank matrix$L$. Due to the compressed background information, there are a few non-zero entries in the sparse matrix$S$. Hence, S shows better sparsity than the original matrix on y-t space, which benefits compressed sensing reconstruction. The sparsity of S can be increased further by applying an appropriate sparsity transform along the matrix columns (temporal dimension) or using adaptive dictionary patches [24], [35], [36]. With a sparser presentation of S, fewer coefficients are required to be recovered, which enables dynamic MRI reconstruction at higher AF.

A variety of dynamic MRI reconstruction frameworks, including GRASP and L+S decomposition, adopted temporal TV as the temporal sparsity transform. Temporal TV applies a finite-differences operator along the temporal dimension of the matrix, minimizing all the variations in the temporal domain. Temporal TV has shown advanced performance for suppressing the under-sampling artifacts [14], [35], but it also suppresses the temporally varied dynamic signal [16]. Temporal FFT is another sparsity transform that can effectively reserve the dynamic contrast. Temporal FFT converted the images series matrix from the y-t domain to the temporal-frequency (y-f) domain by applying an FFT operator along the temporal dimension. In the y-f domain, DC and a few low-frequency components typically occupy most of the power and present the steady background and tissues with relatively slow changes along the temporal dimension,

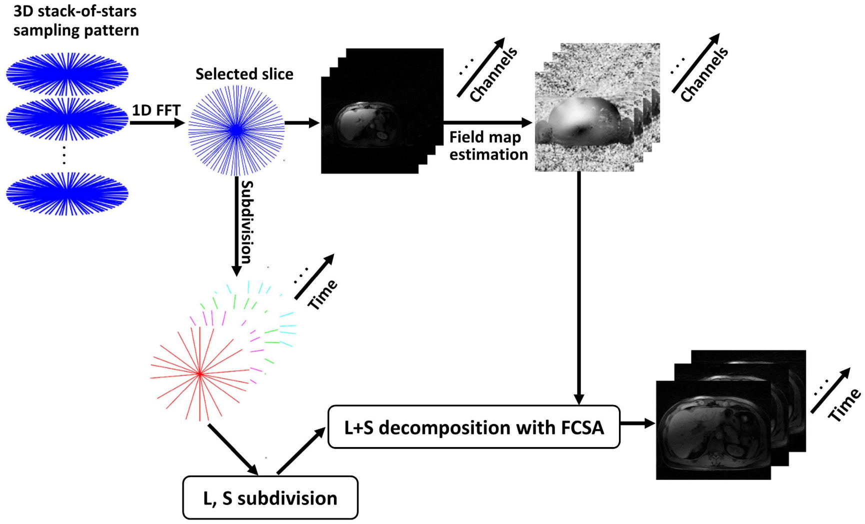

FIGURE 1. **L+S with joint sparsity reconstruction framework. 3D dynamic MRI datasets are typically acquired by the stack-of-stars hybrid sampling pattern. One-dimensional (1D) FFT operator is applied to decompose the 2D slices k-space from the 3D datasets. NUFFT is directly implemented for the selected slice k-space dataset before the time frame subdivision to obtain the reference images. Field maps are estimated from the reference images. Continuously acquired spokes are sorted into multiple frames according to the temporal order. A further subdivision is implemented on time frames to decompose low-rank components and sparse dynamic components in time series. The L+S with joint sparsity Fig. Fig. 1. reconstruction with FCSA is then applied to recover the image series by exploring the temporal sparsity among the dynamic sparse components.**

respectively. Temporal FFT can explore temporal sparsity by gradually eliminating frequency components with negligible magnitude. The DCE signal intensity is assumed to vary temporally at low frequencies. A few low-frequency components are sufficient to catch the relatively smooth variation of signal intensity of blood vessels. These low-frequency components are reserved by temporal FFT to maintain the dynamic contrast. However, the incoherent under-sampling artifacts are distributed among the y-f domain, while the temporal FFT cannot eliminate these artifacts as effectively as temporal TV.

Here, we have introduced an additional sparsity constraint temporal FFT into the standard L+S decomposition model to suppress under-sampling artifacts and recover dynamic contrast simultaneously as:

$$argmin_{L,S} = \frac{1}{2}\left\|\{E\left(L+S\right)-d\}\right\|_2^2 + \lambda_L \left\|\right\|_* + \lambda_T \left\|\right\|_1 + \lambda_F \left\|\right\|_1 \quad (1)$$

d is the acquired multi-coil k-space dataset with c coils while it is highly under-sampled along the temporal dimension of the k-space (k-t space) in dynamic MRI. E is the multi-coil encoding operator, which contains c coils sensitivity maps [37] followed by under-sampled FFT or non-uniform fast Fourier transform (NUFFT) operator. T is the temporal TV sparsity transform which applies the finite-differences operator along the columns of y-t matrix $S.F$ is the temporal FFT transform which applies the FFT operator along the columns of y-t matrix S. $\left\|L\right\|_*$ is the nuclear norm of L, which presents the sum of the singular values of the low-rank matrix. The l_1 norms $\|TS\|_1$and $\|FS\|_1$ present the sum of the absolute value of the entries of S in the temporal TV transform domain and temporal FFT transform domain, respectively. λ_L, λ_F, and λ_T are penalty factors that trade off the data consistency versus the complexity of the solution given by the nuclear norm of L and l_1 norms.

B. FAST COMPOSITE SPLITTING ALGORITHM

The standard L+S decomposition employs the SVD and ISTA to solve the optimization problem and achieves high computation efficiency [24]. Soft-thresholding is consecutively implemented to process the temporal TV constraint to obtain the optimal solution of the L+S decomposition model. The number of gridding/de-gridding procedures is drastically reduced, while the reconstruction efficiency of L+S decomposition is much higher than the standard GRASP. Beck [28] has developed an advanced ISTA algorithm named fast ISTA (FISTA) to accelerate the convergence further. Besides the basic framework of ISTA, FISTA contains a specific linear combination procedure of the previous two iterative stages. Hence, FISTA preserves the computation simplicity of ISTA but with a better convergence rate.

However, both ISTA and FISTA cannot efficiently solve the reconstruction model with multiple L_1 regularizations. To solve the L+S with joint sparsity model, the FCSA [31], [32], a combination of FISTA and composite splitting algorithm (CSA) [38], is employed in this work. CSA is implemented to split the problem with joint sparsity constraints into two sub-problems with a certain

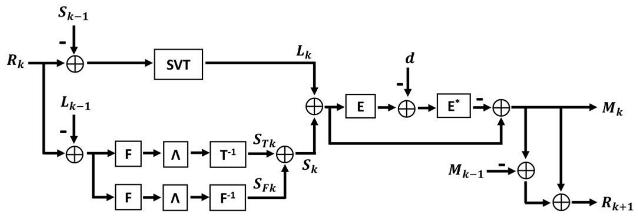

FIGURE 2. **Operation for the kth iteration in L+S decomposition with joint sparsity reconstruction algorithm. R_k, S_k and L_k present the input image matrix, low-rank matrix, and sparse matrix in the kth iteration, respectively. L_k is obtained by applying SVT to $R_k - S_{k-1}$. Two shrinkage operators are implemented to the sparsity constraints in the T and F domains to get S_{Tk} and S_{Fk}, respectively. S_k is figured out by a linear combination of S_{Tk} and S_{Fk}. Image series M_k is then recovered as $M_k = L_k + S_k$. Additional residual signal $E^*(E(L_k + S_k) - d)$ is then subtracted to maintain the data consistency. The updated input R_{k+1} for the next iteration is obtained by a specific linear combination of the current stage M_k and the previous stage M_{k-1} which enforces faster convergence.**

constraint, while the FISTA is used to solve the optimal model efficiently. A linear combination of the solutions of two sub-problems is regarded as the solution for the entire problem.

Figure 2 and Table 1 summarized FCSA for solving the L+S decomposition with joint sparsity model in the proposed method. The input image series matrix M or R is firstly decomposed by an SVD operator as $M = U\Sigma V^H$. A soft-thresholding operator Λ is integrated into the SVD operator to build the SVT operator, applying soft-thresholding for all the singular values as $SVT\ (M) = U\Lambda\ (\Sigma)\ V^H$. The low-rank matrix L is recovered based on the remained singular values, while the dynamic components matrix S is obtained as $S = M - L$.

During the kth iteration, the SVT operator is implemented on $R_k - S_{k-1}$ to obtain the new low-rank matrix L_k. Two temporal sparsity transforms, nT and F, are applied to the sparse components matrix. Another two soft-thresholding operators, Λ_{λ_T} and Λ_{λ_T}, are used to process the sparse matrix in the temporal TV transform domain and temporal FFT transform domain, respectively. Two output sparse matrices, S_{Tk} and S_{Fk}, are obtained as$S_{Tk} = T^{-1}(\Lambda_{\lambda_T}(T(R_k - L_{k-1})))$ and $S_{Fk} = F^{-1}(\Lambda_{\lambda_F}(F(R_k - L_{k-1})))$. The new dynamic components matrix solution is observed as a linear combination of two sparse matrices where $S_k = (S_{Tk} + S_{Fk})/2$ [38]. Consecutively, the output image series M_k is figured out by subtracting $(L_k + S_k)$ with the residual aliasing artifacts $E^*(E(L_k + S_k) - d)$. The input image series matrix for the next iteration R_{k+1} is generated by a linear combination of the current stage output M_k and previous stage output M_{k-1} to achieve fast convergence, followed with specific step sizes t_k and t_{k+1} [32].

C. COMPUTER SIMULATION FRAMEWORK

A computer simulation framework was developed to evaluate the performance of different reconstruction schemes, as shown in Figure 3. A two-dimensional (2D) Shepp-logan computer model with 384 × 384 voxels was designed with dynamic contrast variation. The phantom model consists of three background sections and six dynamic variation sections. The gray level of three background regions was designed as 1, 0.4, and 0.2, respectively, and the signal intensity of these background sections was kept constant, forming the steady background tissues in DCE-MRI. The gray level of dynamic sections is initialized as 0 before the simulation. A dynamic variation curve model was designed based on several clinical DCE-MRI datasets [16], [29], [30]. The virtual time duration of the curve model is 84 s, and its peak occurs at 26.7 s. During Bloch equation simulation, the signal intensity of three dynamic sections was varied with the dynamic curve, simulating the tissues with contrast enhancement in the DCE-MRI.

The Bloch equation simulation was performed using MATLAB 2020b (MathWorks, Natick, MA). During the simulation, the dynamic variation period was uniformly digitalized into 588 discrete time steps with a time gap of 84 s / 588 ≈ 0.14 s. A golden angle radial sampling pattern was applied to acquire phantom datasets. A radial spoke is acquired continuously among these discrete time steps, producing the under-sampled k-space series over the DCE period. An additional fully-sampled k-space dataset is acquired at each time step, forming reference k-space series. Meanwhile, eight exponentially decayed field maps were introduced to modify the signal intensity of the phantom model point by point during simulation, forming eight virtual coils (c=8).

TABLE 1. **L+S with joint sparsity and FCSA for dynamic MRI reconstruction.**

```
L+S with Joint Sparsity Using FCSA
input:
  $d$: multicoil undersampled k-t data
  $E$: multicoil k-t encoding operator
  $T$: temporal total variation sparsity transform
  $F$: temporal fast Fourier sparsity transform
  $\lambda_L$: singular-value threshold
  $\lambda_T$: sparsity threshold for temporal total variation
  $\lambda_F$: sparsity threshold for fast Fourier transform
Initialize: $M_0 = Ed,\ R_1 = M_0,\ S_0 = 0,\ t_1 = 1,$
for $k = 1$ to $K$ do
  $L_k = SVT(R_k - S_{k-1})$
  % soft thresholding in the temporal $T$ domain
  $S_{Tk} = T^{-1}(\Lambda_{\lambda_T}(T(R_k - L_{k-1})))$
  % soft thresholding in the temporal $F$ domain
  $S_{Fk} = F^{-1}(\Lambda_{\lambda_F}(F(R_k - L_{k-1})))$
  % linear combination of solutions for multiple sparsity
  $S_k = (S_{Tk} + S_{Fk})/2$
  % subtract residual for data consistency
  $M_k = L_k + S_k - E^*(E(L_k + S_k) - d)$
  % iteration for the step-size
  $t_{k+1} = (1 + \sqrt{1 + 4\,(t_k)^2}\,)/2$
  % specific linear combination as the next input
  $R_{k+1} = M_k + ((t_k - 1)/t_{k+1})(M_k - M_{k-1})$
end for
output: L, S
```

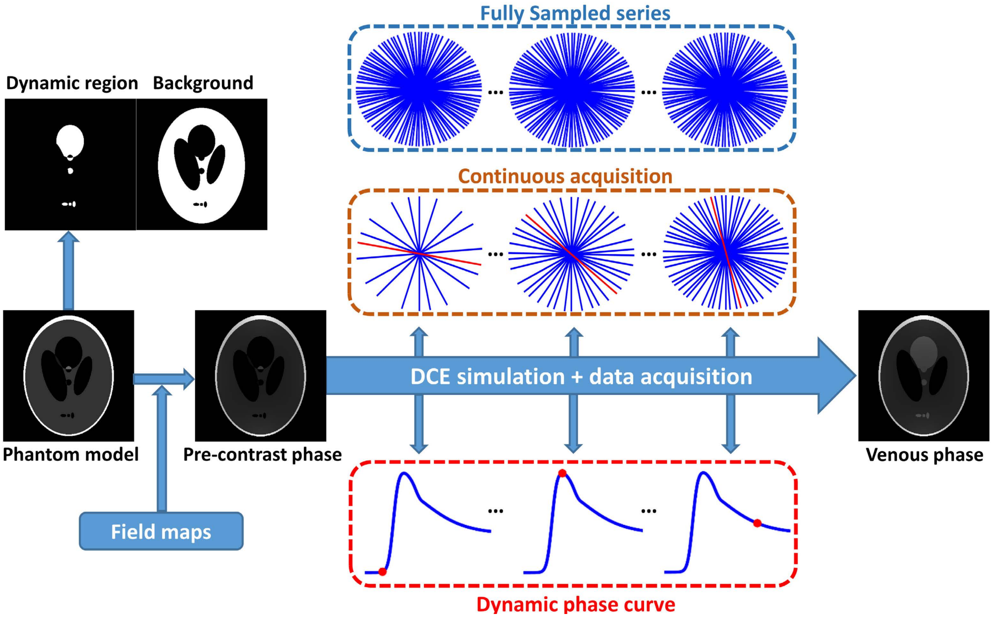

FIGURE 3. Flowchart of data acquisition during dynamic variation period. Eight field maps were integrated into phantom before data acquisition forming multiple virtual coil channels. The simulation of data acquisition contains a total of 588 steps between the pre-contrast phase and the venous phase. Two data acquisitions were executed at each time point, producing a fully sampled reference DCE series and a continuous DCE phantom dataset, respectively.

D. DATA ACQUISITION

T_2 decay and B_0 inhomogeneity are ignored during the computer simulation. A certain radial spoke with 384 sample points was acquired over 588 time steps in 84 s DCE period. The ultimately under-sampled dataset contains eight virtual coils, a total of 588 spokes with 384 readout points within each spoke. An averaging image (without time frame subdivision) was directly reconstructed by a multi-coil NUFFT operator for the estimation of field maps.

In each time step, an additional fully sampled k-space dataset was acquired with 384 readout points and $384 \times \pi/2 = 602$ spokes. Hence, a total of 602×588 spokes were acquired in reference datasets over the dynamic simulation period. The ultimate matrix size for the reference series dataset was $384 \times 602 \times 588$ with eight virtual coils.

A free-breathing liver DCE-MRI dataset provided by Feng [16] was used to evaluate the performance of different reconstruction schemes. The liver dataset was acquired on a healthy volunteer using a stack-of-stars golden angle FLASH pulse sequence. The relevant imaging parameters include TR/TE=3.52 ms/1.41 ms, FOV=380 mm × 380 mm, eight coils, and 588 spokes with 384 readout points each.

E. IMAGE RECONSTRUCTION

The simulation and liver datasets were subdivided into 21 frames with a temporal resolution of 28 spokes/frame. The corresponding AF is 21.5. These two datasets were reconstructed with a matrix size of $384 \times 384 \times 21$ by NUFFT, GRASP, L+S decomposition, and L+S with joint sparsity, respectively. The optimization problem in GRASP was solved using NLCG with 24 iterations. The iteration number for both ISTA and FCSA was set as 20 and used to solve the optimization problem in L+S decomposition and L+S with joint sparsity, respectively. Furthermore, additional reconstructions for these three schemes were performed on the liver dataset with a temporal resolution of 14 spokes/frame and 21 spokes/frame to test the robustness of L+S based techniques for highly under-sampled reconstruction.

All the reconstructions were performed using MATLAB 2020b (MathWorks, Natick, MA) on an Intel Core i7-10700 PC with a 2.9 GHz processor. The reconstructions of three schemes were repeated ten times to evaluate their reconstruction efficiency accurately.

F. RECONSTRUCTION PARAMETER DESIGN

The weighting factors of sparsity constraints directly determine the image quality of the reconstructed series. The regularization parameters of Temporal TV λ_T in GRASP, L+S decomposition, and L+S with joint sparsity were set the same for a fair comparison. A variety of GRASP and L+S decomposition reconstructions were executed with the different λ_T ranging from $0.1 \times M_s$ to $0.8 \times M_s$ (step size 0.05), where M_s presents the maximum magnitude of the images series directly reconstructed by the multi-coil NUFFT operator. According to the evaluation of image quality from two experienced radiologists, an optimized value $\lambda_T = 0.2 \times M_s$ was implemented for all three reconstruction schemes. λ_L in the proposed method followed the same setup as in the L+S decomposition model.

Similar to the design of λ_T, different values of λ_F were combined with the other two regularization parameters in L+S with joint sparsity. An adequate value of λ_F was

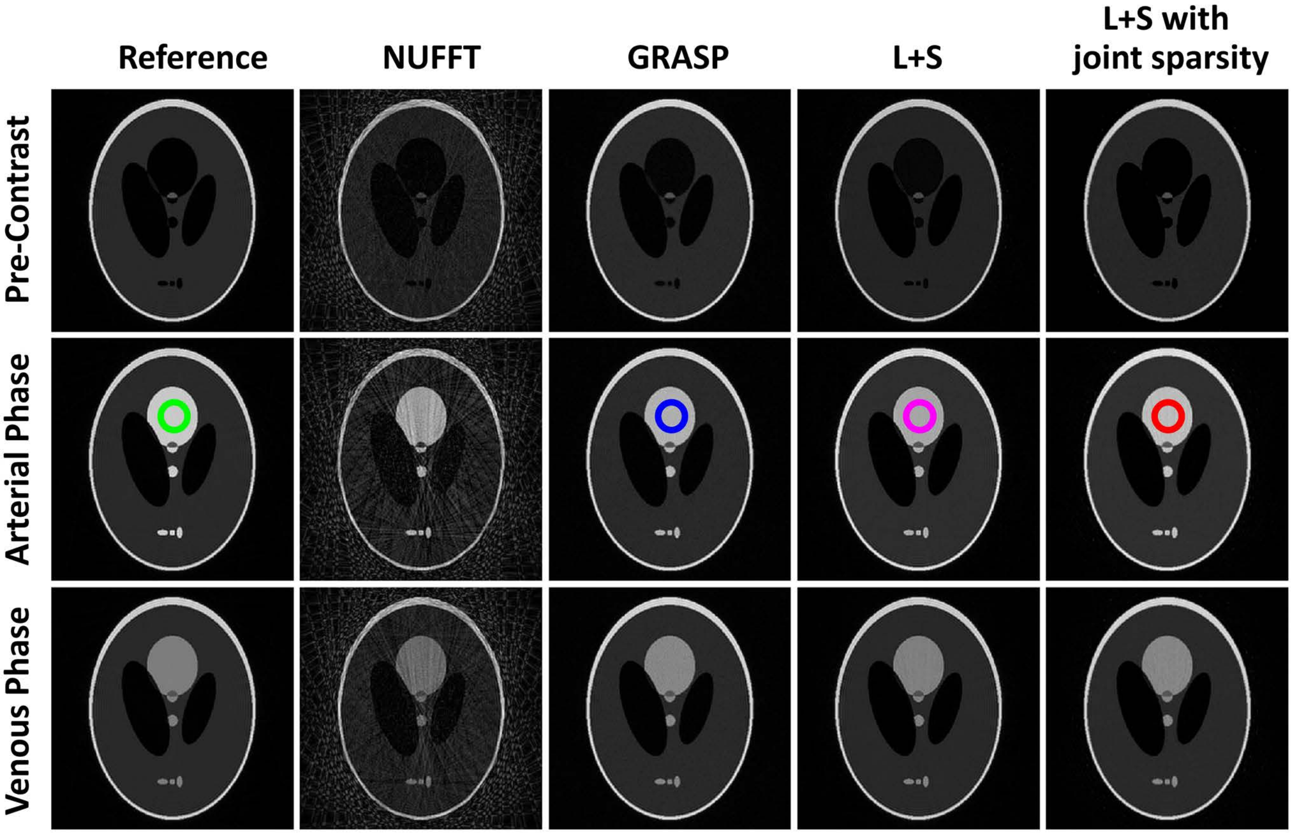

FIGURE 4. **Three phase images corresponding to the reconstruction of the simulated phantom dataset with AF = 21.5 (588 radial spokes and temporal resolution of 28 spokes/frame) using NUFFT, GRASP, L+S decomposition, and the proposed method (L+S with joint sparsity and FCSA). Signal intensity in the selected region (labeled by circles) among all the frames was used to estimate the dynamic contrast performance in different reconstruction schemes.**

designed for reconstruction with a specific temporal resolution by testing different values and comparing the image quality as well as dynamic contrast signal intensity (ultimately selected by experienced radiologists). Besides the regularization parameters, other reconstruction parameters in GRASP, L+S decomposition, and L+S with joint sparsity were carefully followed by their initial setups [16], [24].

III. RESULTS AND DISCUSSION

A. DYNAMIC CONTRAST AND RECONSTRUCTION EFFICIENCY

Figure 4 shows three contrast phases of the simulated Shepp-logan phantom images reconstructed by GRASP, standard L+S decomposition, and L+S with joint sparsity, respectively. The gray level of all reconstruction results has been normalized according to the mean value of steady background sections for comparing the dynamic contrast. All three reconstruction schemes successfully removed undersampling artifacts. The dynamic contrast in the selected region was visually degraded in three reconstruction schemes compared to the reference image.

Figure 5 and Table 2 present the average reconstruction time and corresponding dynamic performance of the three schemes in the phantom dataset. With the support of FCSA, a slight increase of 3% computation cost was caused by an additional sparsity constraint in the proposed method compared to standard L+S decomposition. Both two L+S based frameworks achieved similar reconstruction efficiency by using only about 25% of computation time for GRASP. There was no obvious dynamic degradation obtained in the fully sampled reference series. The peak of the dynamic signal was

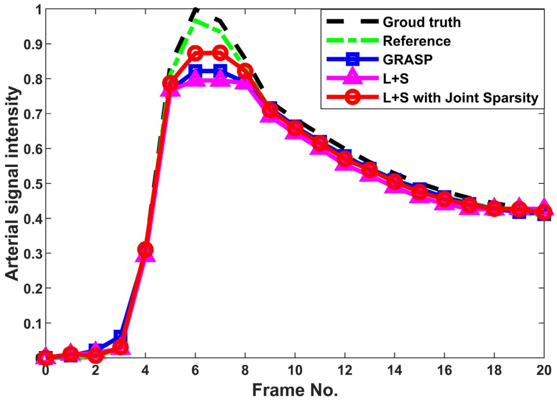

FIGURE 5. **Dynamic signal variation for the phantom using ground truth, fully sampled reference, GRASP, L+S, and L+S with joint sparsity. Using the ground truth and fully sampled reference as the benchmark, our proposed L+S with joint sparsity method demonstrated much better dynamic contrast compared with GRASP and standard L+S.**

TABLE 2. Reconstruction time, RMSE, peak DCE signal, and mean DCE signal of the three reconstruction schemes in the simulated phantom data. Reconstruction efficiency has been significantly improved in the proposed method due to L+S reconstruction, while joint sparsity improved dynamic contrast in the proposed method.

Reconstruction Scheme	Euclidean Distance	Reconstruction Time (s)	Peak DCE Signal	Mean DCE Signal	RMSE
Reference	0.0829	-	0.9675	0.4832	-
GRASP	0.2557	490	0.8225	0.4701	0.0289
L+S decomposition	0.306	111	0.7959	0.4575	0.0331
Proposed method	0.1819	114	0.8747	0.4742	0.0221

degraded by only 3.3% in reference, proving the dynamic robustness of fully sampling. The peak of the dynamic signal was degraded by 17.6% and 20.3% for GRASP and the standard L+S method compared to the reference. The best dynamic contrast was achieved by the proposed reconstruction scheme. The peak of the dynamic signal was only degraded by 12.4% in the proposed method, which is much lower than the standard L+S decomposition. Using the reference series as the standard, we have calculated the root mean square error (RMSE) of three reconstruction schemes in the arterial phase. The degradation of the dynamic signal caused the largest RMSE value in the standard L+S model. Using the dynamic curve model as the benchmark, the Euclidean distance of the proposed method is only 0.182, which is much smaller than the 0.256 for GRASP and 0.306 for the standard L+S method, suggesting that our method can capture the dynamic arterial signals much better.

Figure 6 shows a comparison of different reconstruction schemes in the three representative contrast phases in a free-breathing liver DCE-MRI dataset. Two L+S based techniques present a better background structure of the liver. A better dynamic contrast of tissues (labeled by solid arrows) was observed in GRASP and the proposed method. Dynamic blurring was observed in standard L+S reconstruction (labeled by dashed arrows) due to the degradation of dynamic contrast. The reconstruction period for the liver dataset was typically larger than that for the simulated phantom dataset. The average reconstruction time for GRASP, L+S decomposition, and L+S with joint sparsity is 705 s, 182 s, and 185 s, respectively. Two L+S based reconstruction schemes still achieved around four times faster reconstruction speed than the GRASP method. The extension of the reconstruction period in the proposed method is still negligible compared with standard L+S decomposition.

Figure 7 shows the dynamic signal variation in the selected arterial region in GRASP, L+S decomposition, and L+S with joint sparsity for the liver DCE-MRI dataset. The peak dynamic signal in the liver dataset in the proposed method demonstrated an increase in peak dynamic DCE signal by 24.8% and 33% than that of GRASP and standard L+S methods, respectively. Clear improvement of dynamic contrast was achieved by utilizing joint sparsity constraints in the proposed method.

Figure 8 demonstrates a further comparison of three reconstruction schemes in the venous phase at different AF=22, 29, and 43 in the liver DCE-MRI dataset. Blurring artifacts degrade the tissue contrast in GRASP at AF=43. The detail of abdomen tissues is not degraded significantly in L+S decomposition and L+S with joint sparsity. The L+S based schemes show the robustness for highly under-sampled dataset reconstruction.

B. PERFORMANCE ANALYSIS

The stack-of-stars golden angle radial sampling satisfies well the requirement for temporal compressed sensing [39]. A continuous data acquisition model can cover the whole dynamic variation period. Then the acquired spokes are subdivided into multiple time frames according to the temporal acquisition order. The sub-sampling patterns among time frames are completely different, which induces incoherent streaking artifacts among the time series. In radial sampling, the k-space center is acquired repeatedly, while the image contrast of radial sampling corresponds to the average over the acquisition window. This temporal averaging effect offers intrinsic motion robustness but degrades the dynamic contrast to some extent.

Temporal TV is a robust sparsity transform and is widely adopted in dynamic reconstruction frameworks, including GRASP and L+S decomposition. However, temporal TV aims to minimize all the variations along the temporal dimension. Additional temporal averaging was induced by temporal TV, leading to unexpected dynamic contrast degradation. With the same penalty factor design, L+S decomposition experienced more dynamic degradation. The temporal averaging effect is directly related to the penalty factor design of Temporal TV. With the increase of penalty factor, both GRASP and L+S decomposition can achieve better artifact suppression but with worse dynamic contrast.

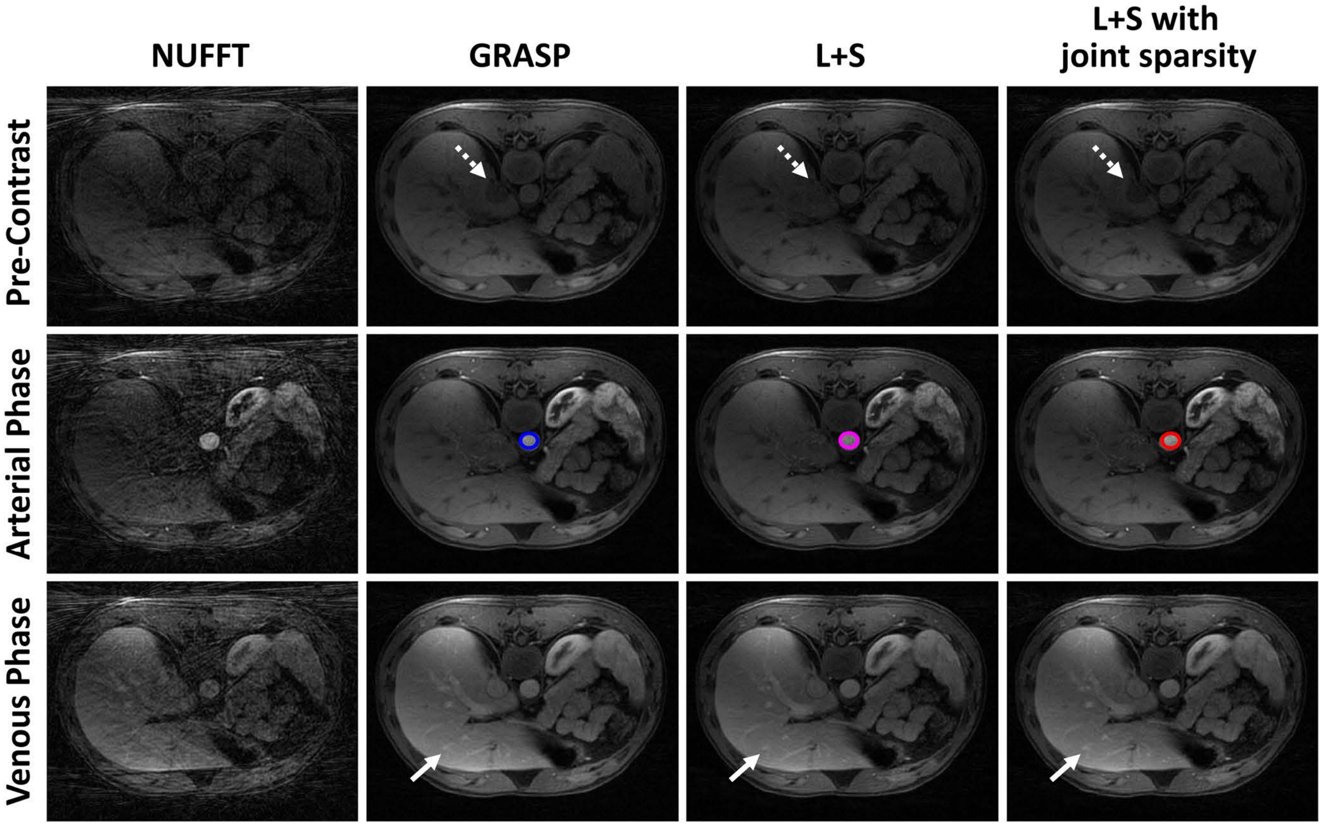

FIGURE 6. A comparison of different reconstruction schemes in the three representative phases in a liver DCE-MRI dataset at AF = 22 and 28 spokes/frame. Both the proposed method and the standard L+S method provide better background structures than GRASP. Our L+S with joint sparsity followed by Fig. Fig. 1. FCSA demonstrated better dynamic contrast (solid arrow and dashed arrow). Arterial signal intensity in the selected region (labeled by circles) among all the frames was used to estimate the dynamic contrast performance in different reconstruction schemes.

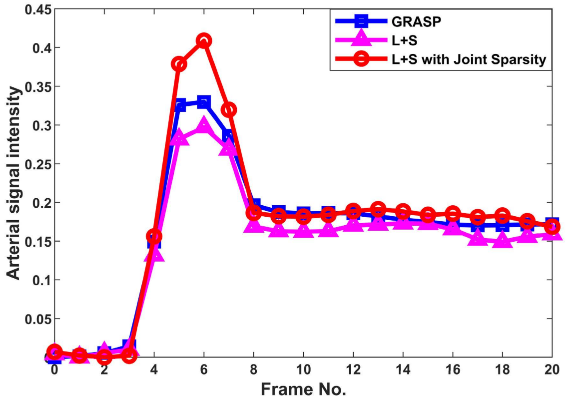

FIGURE 7. Dynamic signal variation in the arterial region for the liver DCE-MRI dataset by using GRASP, L+S, and L+S with joint sparsity. Improved dynamic contrast was achieved by our proposed L+S with joint sparsity. Significant improvement of peak dynamic signal was observed in the proposed L+S with joint sparsity.

To recover the dynamic contrast from temporal blurring, temporal FFT has been proposed in combination with temporal TV to explore the temporal sparsity among subdivided time series. The proposed L+S with joint sparsity can still suppress the streaking artifacts effectively by temporal TV. In the temporal FFT transform domain, the frequency components with negligible magnitude are gradually filtered out during the iterative reconstruction. The remaining frequency components are sufficient to recover the dynamic variation accurately, enabling improved dynamic contrast. Compared with GRASP and L+S decomposition, significant improvement in dynamic contrast was obtained in the proposed method in reconstructing different datasets, showing the robustness of temporal FFT for recovering dynamic contrast.

Besides the dynamic contrast, reconstruction efficiency is crucial for online clinical applications. The reconstruction efficiency of GRASP is relatively low due to the repeated gridding/de-gridding procedures in NLCG. Compared with GRASP, L+S decomposition shows a little bit worse dynamic contrast but much better reconstruction efficiency. The number of gridding/de-gridding procedures is reduced significantly by ISTA. In the proposed method, the additional sparsity constraint leads to an increase in computation complexity. The FCSA decomposes the optimization problem with joint sparsity constraints into multiple sub-problems with a single sparsity constraint to reduce the computation complexity. The linear combination of the output of sub-problems can recover the image series more effectively. With

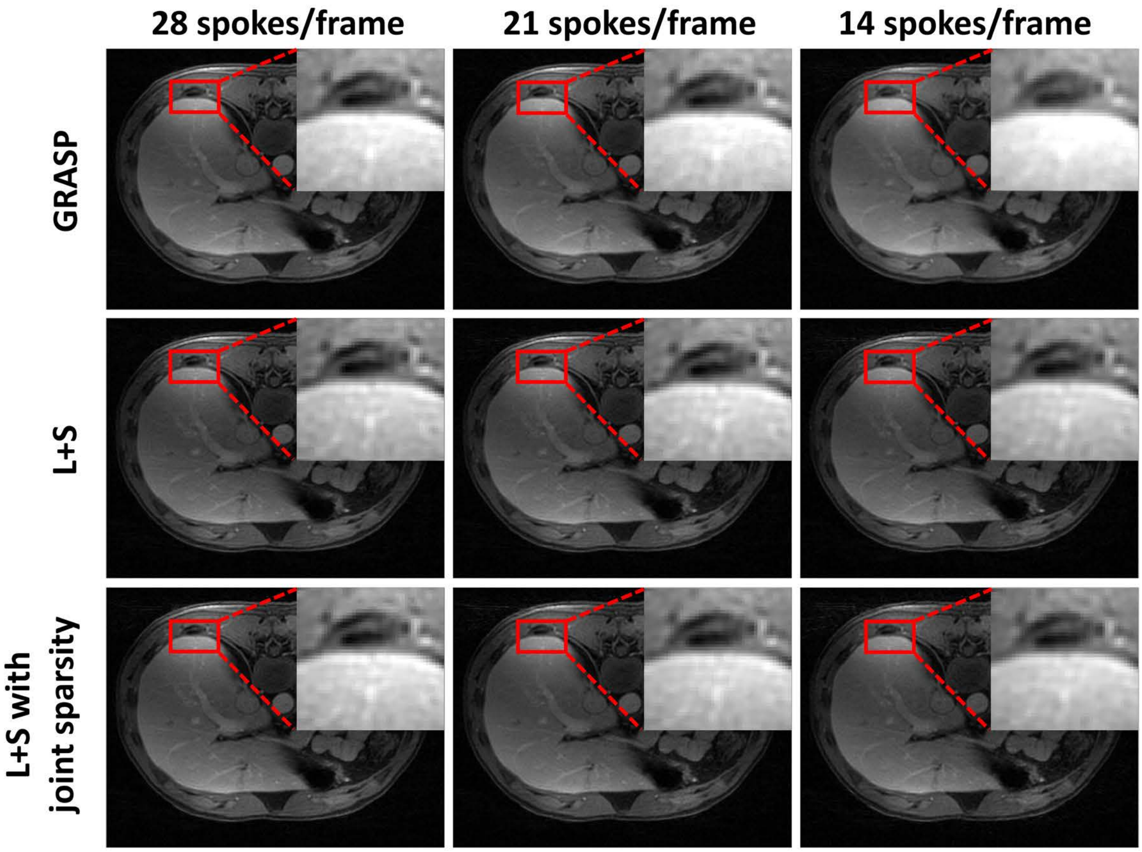

FIGURE 8. **A comparison of the reconstructed images of GRASP, L+S decomposition, and L+S with joint sparsity at different temporal resolutions in the venous phase of the liver DCE-MRI dataset. A total of 21, 28, and 42 frames were reconstructed at different temporal resolutions, respectively. In the zoomed view of the liver section, blurring artifacts and degradation of tissue contrast were observed in GRASP. Less blurring artifacts and degradation were observed in L+S with joint sparsity. The penalty factor for the three reconstruction schemes was set the same among all the reconstructions.**

the support of FCSA, the computation cost from the temporal FFT is negligible. Both standard L+S decomposition and the proposed L+S based methods achieved around four times faster reconstruction speed than the GRASP method.

The performance of DCE-MRI reconstruction is typically evaluated visually by experienced radiologists. There are no standard evaluation criteria for quantifying the performance of different reconstruction schemes. Hence, a computer simulation framework was developed here. The benefit of computer simulation is that the ground truth, like dynamic signal variation, can be simulated and obtained. The dynamic performance of the proposed method and other reconstruction schemes can be compared and evaluated by the parameters like Euclidean distance and magnitude of the dynamic signal. The minimum degradation of peak dynamic signal and Euclidean distance were obtained in the proposed method, demonstrating the feasibility of the proposed computer simulation framework for evaluating the dynamic contrast quantitatively.

IV. CONCLUSION

L+S with joint sparsity demonstrates the use of combining the L+S model with joint sparsity constraints for improved dynamic contrast, high temporal resolution, and computationally efficient free-breathing DCE-MRI. The improvement of dynamic contrast provides better image quality and tissue contrast which benefits the clinical diagnosis. The use of the FCSA algorithm minimized the computation cost caused by the additional sparsity constraint. The proposed reconstruction framework can be accelerated further by combining some computer acceleration techniques like parallel computing and enabling a wide range of online clinical applications.

REFERENCES

[1] M. Usman, D. Atkinson, F. Odille, C. Kolbitsch, G. Vaillant, T. Schaeffter, P. G. Batchelor, and C. Prieto, "Motion corrected compressed sensing for free-breathing dynamic cardiac MRI," *Magn. Reson. Med.*, vol. 70, no. 2, pp. 504–516, Aug. 2013.

[2] A. R. Padhani, "Dynamic contrast-enhanced MRI in clinical oncology: Current status and future directions," *J. Magn. Reson. Imag.*, vol. 16, no. 4, pp. 407–422, Oct. 2002.

[3] S. P. Sourbron and D. L. Buckley, "Classic models for dynamic contrast-enhanced MRI," *NMR. Biomed.*, vol. 26, no. 8, pp. 1004–1027, Aug. 2013.

[4] R. Alonzi, A. R. Padhani, and C. Allen, "Dynamic contrast enhanced MRI in prostate cancer," *3 Eur. Radiol.*, vol. 63, no. 3, pp. 335–350, Sep. 2007.

[5] B. Xu, P. Spincemaille, G. Chen, M. Agrawal, T. D. Nguyen, M. R. Prince, and Y. Wang, "Fast 3D contrast enhanced MRI of the liver using temporal resolution acceleration with constrained evolution reconstruction," *Magn. Reson. Med.*, vol. 69, no. 2, pp. 370–381, 2013.

[6] P. Sujlana, J. Skrok, and L. M. Fayad, ''Review of dynamic contrast-enhanced MRI: Technical aspects and applications in the musculoskeletal system,'' *J. Magn. Reson. Imag.*, vol. 47, no. 4, pp. 875–890, Apr. 2018.

[7] T. E. Yankeelov and J. C. Gore, ''Dynamic contrast enhanced magnetic resonance imaging in oncology: Theory, data acquisition, analysis, and examples,'' *Curr. Med. Imag.*, vol. 3, no. 2, pp. 91–107, May 2009.

[8] K. P. Pruessmann, M. Weiger, M. B. Scheidegger, and P. Boesiger, ''SENSE: Sensitivity encoding for fast MRI,'' *Magn. Reson. Med.*, vol. 42, no. 5, pp. 952–962, 1999.

[9] M. A. Griswold, P. M. Jakob, R. M. Heidemann, M. Nittka, V. Jellus, J. Wang, B. Kiefer, and A. Haase, ''Generalized autocalibrating partially parallel acquisitions (GRAPPA),'' *Magn. Reson. Med.*, vol. 47, no. 6, pp. 1202–1210, 2002.

[10] M. A. Ohliger, A. K. Grant, and D. K. Sodickson, ''Ultimate intrinsic signal-to-noise ratio for parallel MRI: Electromagnetic field considerations,'' *Magn. Reson. Med.*, vol. 50, no. 5, pp. 1018–1030, Nov. 2003.

[11] M. Lustig, D. L. Donoho, J. M. Santos, and J. M. Pauly, ''Compressed sensing MRI,'' *IEEE Signal Process. Mag.*, vol. 25, no. 2, pp. 72–82, Mar. 2008.

[12] M. Lustig, D. Donoho, and J. M. Pauly, ''Sparse MRI: The application of compressed sensing for rapid MR imaging,'' *Magn. Reson. Med.*, vol. 58, no. 6, pp. 1182–1195, 2007.

[13] D. Kim, H. A. Dyvorne, R. Otazo, L. Feng, D. K. Sodickson, and V. S. Lee, ''Accelerated phase-contrast cine MRI using k-t SPARSE-SENSE,'' *Magn. Reson. Med.*, vol. 67, no. 4, pp. 1054–1064, Apr. 2012.

[14] L. Feng, M. B. Srichai, R. P. Lim, A. Harrison, W. King, G. Adluru, E. V. Dibella, D. K. Sodickson, R. Otazo, and D. Kim, ''Highly accelerated real-time cardiac cine MRI using k-t SPARSE-SENSE,'' *Magn. Reson. Med.*, vol. 70, no. 1, pp. 64–74, Jul. 2013.

[15] K. T. Block, M. Uecker, and J. Frahm, ''Undersampled radial MRI with multiple coils. Iterative image reconstruction using a total variation constraint,'' *Magn. Reson. Med.*, vol. 57, pp. 1086–1098, Jun. 2007.

[16] L. Feng, R. Grimm, K. T. Block, H. Chandarana, S. Kim, J. Xu, L. Axel, D. K. Sodickson, and R. Otazo, ''Golden-angle radial sparse parallel MRI: Combination of compressed sensing, parallel imaging, and golden-angle radial sampling for fast and flexible dynamic volumetric MRI,'' *Magn. Reson. Med.*, vol. 72, no. 3, pp. 707–717, Sep. 2014.

[17] Z. Zhou, F. Han, L. Yan, D. J. J. Wang, and P. Hu, ''Golden-ratio rotated stack-of-stars acquisition for improved volumetric MRI,'' *Magn. Reson. Med.*, vol. 78, no. 6, pp. 2290–2298, Dec. 2017.

[18] S. Winkelmann, T. Schaeffter, T. Koehler, H. Eggers, and O. Doessel, ''An optimal radial profile order based on the golden ratio for time-resolved MRI,'' *IEEE Trans. Med. Imag.*, vol. 26, no. 1, pp. 68–76, Jan. 2007.

[19] Y.-H. Dai and Y. Yuan, *Nonlinear Conjugate Gradient Methods*. Shanghai, China: Shanghai Sci Technology, 2000.

[20] A. B. Rosenkrantz, C. Geppert, R. Grimm, T. K. Block, C. Glielmi, L. Feng, R. Otazo, J. M. Ream, M. M. Romolo, S. S. Taneja, D. K. Sodickson, and H. Chandarana, ''Dynamic contrast-enhanced MRI of the prostate with high spatiotemporal resolution using compressed sensing, parallel imaging, and continuous golden-angle radial sampling: Preliminary experience,'' *J. Magn. Reson. Imag.*, vol. 41, no. 5, pp. 1365–1373, May 2015.

[21] H. Chandarana, L. Feng, T. K. Block, A. B. Rosenkrantz, R. P. Lim, J. S. Babb, D. K. Sodickson, and R. Otazo, ''Free-breathing contrast-enhanced multiphase MRI of the liver using a combination of compressed sensing, parallel imaging, and golden-angle radial sampling,'' *Investigative Radiol.*, vol. 48, no. 1, pp. 10–16, Jan. 2013.

[22] T. Benkert, Y. Tian, C. Huang, E. V. R. DiBella, H. Chandarana, and L. Feng, ''Optimization and validation of accelerated golden-angle radial sparse MRI reconstruction with self-calibrating GRAPPA operator gridding,'' *Magn. Reson. Med.*, vol. 80, no. 1, pp. 286–293, Jul. 2018.

[23] S. G. Lingala, Y. Hu, E. DiBella, and M. Jacob, ''Accelerated dynamic MRI exploiting sparsity and low-rank structure: Kt SLR,'' *IEEE Trans. Med. Imag.*, vol. 30, no. 5, pp. 1042–1054, May 2011.

[24] R. Otazo, E. Candès, and D. K. Sodickson, ''Low-rank plus sparse matrix decomposition for accelerated dynamic MRI with separation of background and dynamic components,'' *Magn. Reson. Med.*, vol. 73, no. 3, pp. 1125–1136, Mar. 2015.

[25] K. H. Jin, D. Lee, and J. C. Ye, ''A general framework for compressed sensing and parallel MRI using annihilating filter based low-rank Hankel matrix,'' *IEEE Trans. Comput. Imag.*, vol. 2, no. 4, pp. 480–495, Dec. 2016.

[26] V. Chandrasekaran, S. Sanghavi, P. A. Parrilo, and A. S. Willsky, ''Rank-sparsity incoherence for matrix decomposition,'' *SIAM J. Optim.*, vol. 21, no. 2, pp. 572–596, 2011.

[27] E. J. Candès, X. Li, Y. Ma, and J. Wright, ''Robust principal component analysis?'' *J. ACM*, vol. 58, no. 3, pp. 1–37, May 2011.

[28] A. Beck and M. Teboulle, ''A fast iterative shrinkage-thresholding algorithm for linear inverse problems,'' *SIAM J. Imag. Sci.*, vol. 2, no. 1, pp. 183–202, 2009.

[29] L. Feng, L. Axel, H. Chandarana, K. T. Block, D. K. Sodickson, and R. Otazo, ''XD-GRASP: Golden-angle radial MRI with reconstruction of extra motion-state dimensions using compressed sensing,'' *Magn. Reson. Med.*, vol. 75, no. 2, pp. 775–788, Feb. 2016.

[30] L. Feng, C. Huang, K. Shanbhogue, D. K. Sodickson, H. Chandarana, and R. Otazo, ''RACER-GRASP: Respiratory-weighted, aortic contrast enhancement-guided and coil-unstreaking golden-angle radial sparse MRI,'' *Magn. Reson. Med.*, vol. 80, no. 1, pp. 77–89, Jul. 2018.

[31] J. Huang, S. Zhang, and D. Metaxas, ''Efficient MR image reconstruction for compressed MR imaging,'' *Med. Image Anal.*, vol. 15, no. 5, pp. 670–679, Oct. 2011.

[32] J. Huang, L. Wang, and Y. Zhu, ''Compressed sensing MRI reconstruction with multiple sparsity constraints on radial sampling,'' *Math. Problems Eng.*, vol. 2019, pp. 1–14, Feb. 2019.

[33] J. Zhang, ''Improved ultrashort time echo and dynamic contrast enhancement magnetic resonance imaging based on Stack-of-Stars golden angle radial sampling scheme,'' Ph.D. dissertation, Dept. Electr. Electron. Eng., Univ. Nottingham Ningbo China, Ningbo, China, 2022.

[34] S. G. Lingala, Y. Hu, E. DiBella, and M. Jacob, ''Accelerated dynamic MRI exploiting sparsity and low-rank structure: K-t SLR,'' *IEEE Trans. Med. Imag.*, vol. 30, no. 5, pp. 1042–1054, May 2011.

[35] L. Chen, M. C. Schabel, and E. V. DiBella, ''Reconstruction of dynamic contrast enhanced magnetic resonance imaging of the breast with temporal constraints,'' *Magn. Reson. Imag.*, vol. 28, no. 5, pp. 637–645, 2010.

[36] S. Ravishankar, B. E. Moore, R. R. Nadakuditi, and J. A. Fessler, ''Low-rank and adaptive sparse signal (LASSI) models for highly accelerated dynamic imaging,'' *IEEE Trans. Med. Imag.*, vol. 36, no. 5, pp. 1116–1128, May 2017.

[37] D. O. Walsh, A. F. Gmitro, and M. W. Marcellin, ''Adaptive reconstruction of phased array MR imagery,'' *Magn. Reson. Med.*, vol. 43, no. 5, pp. 682–690, 2000.

[38] J. Huang, S. Zhang, H. Li, and D. Metaxas, ''Composite splitting algorithms for convex optimization,'' *Comput. Vis. Image Understand.*, vol. 115, no. 12, pp. 1610–1622, 2011.

[39] L. Feng, ''Golden-angle radial MRI: Basics, advances, and applications,'' *J. Magn. Reson. Imag.*, vol. 56, no. 1, pp. 45–62, Jul. 2022.

JICHANG ZHANG received the B.S. degree in electrical and electronic engineering from the University of Nottingham Ningbo China, in 2015, the M.S. degree in electronic communication and computer engineering from the University of Nottingham, U.K., in 2016, and the Ph.D. degree from the University of Nottingham Ningbo China, China, in 2022. His research interests include dynamic MRI, pulse sequence development, and acceleration techniques for image reconstruction.

FAISAL NAJEEB received the Ph.D. degree in medical imaging from COMSATS University Islamabad, Pakistan, in 2021, the Postgraduate Research from SPMIC University of Nottingham U.K. as a part of his Ph.D. research, in 2020. He is currently working as a Lecturer with the Department of Electrical Engineering, COMSATs University Islamabad. He is an Active Member at the Medical Image Processing Research Group (MIPRG), COMSATs University Islamabad. His research interests include MR image reconstruction, cardiac MRI, and deep-learning techniques for dynamic MRI.

XINPEI WANG received the B.S. and Ph.D. degrees in electrical and electronic engineering from the University of Nottingham Ningbo China, in 2017 and 2022, respectively. His research interests include MR image reconstruction, T1 mapping, pulse sequence development, new hyperpolarizer techniques, and hyperpolarized Xe application.

PENGFEI XU received the B.E. degree in automation from Xian Technological University, Xi'an, China, in 2015, and the M.S. degree in control science and engineering from the University of Science and Technology Beijing, Beijing, China, in 2018. She is currently pursuing the Ph.D. degree in electrical and electronic engineering with the University of Nottingham, Ningbo, China. Her research interests include MRI sequences, image reconstruction, and oxygen-enhanced lung MRI.

HAMMAD OMER received the M.S. and Ph.D. degrees from Imperial College London, U.K. He is currently a Group Leader with the Medical Image Processing Research Group (MIPRG), COMSATs University Islamabad. He is also working on the optimization of medical image reconstruction algorithms for an efficient implementation on FPGA and GPUs. More than ten students have completed Ph.D. under his supervision in MRI imaging. His research interests include MRI image reconstruction, diffusion-weighted MRI, cardiac MRI, and AI-based MR Image reconstruction.

JIANJUN ZHENG received the B.M. degree in clinical medicine from Zhejiang University, China, in 2003, and the M.S. degree from the University of Hong Kong, in 2007. He is currently working as a Doctoral Tutor with Ningbo University, China. He is also the Director at Ningbo Hwamei Hospital, University of Chinese Academy of Sciences (Ningbo Second Hospital). With 28 years of clinical experience, he is an expert in the early diagnosis of tumors, multidisciplinary collaboration, the formulation of individualized diagnosis, and treatment plans. His research interests include clinical imaging, molecular imaging in the tumor, cardiovascular direction, and new imaging materials.

JINGFENG ZHANG received the Ph.D. degree in image medicine and nuclear medicine from Tongji Medical College, Huazhong University of Science and Technology, in 2005. He is the Chief Physician with the Radiology Department, Chief of the Education Section, and the Director of the Diagnosis and Treatment Center, Ningbo Hwamei Hospital, University of Chinese Academy of Sciences (Ningbo Second Hospital). His research interests include imaging diagnosis and interventional treatment of complicated diseases, intelligent imaging, and intelligent medical education.

SUE FRANCIS is currently a Professor of physics at the Faculty of Science, University of Nottingham. She has developed/implemented arterial spin labeling (ASL) methods to non-invasively measure blood flow and blood volume in the brain. Her research interests include developing magnetic resonance imaging (MRI) methods for biomedical applications, the application and development of functional magnetic resonance imaging (fMRI) techniques in neuroscience, and the development of quantitative MRI methods.

PAUL GLOVER is currently working as an Associate Professor of physics with the Faculty of Science, University of Nottingham, U.K. His research interests include developments and applications of magnetic resonance imaging which include the design of radio-frequency probes to generate the required excitation fields, and the safety of magnetic fields and their interaction with the human body.

RICHARD BOWTELL received the degree in natural science from the University of Cambridge, and the Ph.D. degree from the University of Nottingham, in 1984. He is the Head of the School of physics and astronomy, University of Nottingham. His research is carried out at the Sir Peter Mansfield Magnetic Resonance Centre. His research interests include developing improved equipment and techniques for magnetic resonance imaging and applying them in biomedical studies, and the spatiotopic mapping of human-brain function using ultra-high-field MRI.

CHENGBO WANG received the B.S. and M.S. degrees in biomedical engineering from Tsinghua University, and the Ph.D. degree from the University of Virginia, in 2007. He is currently an Associate Professor with the University of Nottingham Ningbo China. His research interests include theoretical and experimental development of new magnetic resonance imaging techniques to meet the research and clinical needs of the medical and biomedical community, MRI hardware, optimization of the MRI pulse sequences, MRI physics, and hyperpolarized noble-gases MRI.

• • •